

Investigation on Phase Stability of $\text{Al}_x\text{Co}_{0.2}\text{Cr}_{0.2}\text{Ni}_{0.2}\text{Ti}_{0.4-x}$ High Entropy Alloys

Yunhao Zhao¹ · Yusheng Yang¹ · Chia-Hsien Lee¹ · Wei Xiong¹ 

Submitted: 1 May 2018 / in revised form: 13 June 2018
© ASM International 2018

Abstract Phase stability of $\text{Al}_x\text{Co}_{0.2}\text{Cr}_{0.2}\text{Ni}_{0.2}\text{Ti}_{0.4-x}$ ($x = 0.1, 0.2$ or 0.3 , in mole fraction) high entropy alloys (HEAs) in both as-cast and as-annealed states is studied through thermodynamic calculations and experimental characterization. Both disordered bcc_A2 and ordered bcc_B2 phases are observed in the as-cast alloys and exhibit rather high stability with slow diffusion kinetics during post-annealing. Influences of Al/Ti content ratio on lattice constant, phase stability and hardness are discussed through comparison between computation and experiments. It is found that higher Al/Ti ratio stabilizes phases dramatically for both bcc_A2 and bcc_B2 phases, which are observed in all three as-cast $\text{Al}_x\text{Co}_{0.2}\text{Cr}_{0.2}\text{Ni}_{0.2}\text{Ti}_{0.4-x}$ HEAs. The comparison between calculation of phase diagrams (CALPHAD) model prediction and experimental results indicates a promising approach to design HEAs by applying the CALPHAD database. Moreover, the current CALPHAD database still needs to be further improved for a reliable parametric design of alloy composition and post-heat treatment.

Keywords alloy thermodynamics · high entropy alloys · microstructure · phase stability

1 Introduction

HEAs constitute a newly-emerging class of materials, which are typically comprised of five or more principal elements with the atomic percentage of 5–35% for each.^[1] Due to high configurational entropy with induced high stability, such alloys often favor solid solution formation over competing intermetallic compounds. Therefore, there is a high chance to observe basic crystal structures in the alloys such as body centered cubic (bcc), face centered cubic (fcc), hexagonal close packed (hcp), mixture of the above, or solid solution phases co-existing with other intermetallic compounds.^[2] Some HEAs are developed with superior properties, for example, outstanding mechanical strength with good ductility, and high corrosion resistance.^[2–9] Among these studied HEAs, the Al-Co-Cr-Fe-Ni system has been investigated by many researchers due to its potential in high-temperature high-strength applications.^[10] It is generally believed that Co and Ni are essential for high temperature structural materials,^[11–13] while Cr and Al are necessary to enhance corrosion resistance.^[14–16] Al is able to influence the phase formation and acts as bcc phase stabilizer.^[17–19] The Al-Co-Cr-Fe-Ni equiatomic HEAs are found to have disordered bcc_A2 and ordered bcc_B2 phases after annealing.^[14] Furthermore, Wang et al.^[17] investigated the phase formation in as-cast $\text{Al}_x\text{CoCrFeNi}$ ($x = 0–0.2$, in molar ratio) alloys and found the content of Al can influence the phase formation. A dual-phase microstructure with the mixture of bcc_A2 and bcc_B2 is observed in alloys when x is between 0.9 and 2.0. Besides, the alloy $\text{Al}_{0.9}\text{CoCrFeNi}$ is found to exhibit the highest hardness due to its fine microstructure introduced by spinodal decomposition.

Although the addition of Fe may reduce the cost and result in higher stability of bcc structure, it is intriguing to

✉ Wei Xiong
wxiong@yahoo.com; weixiong@pitt.edu

¹ Physical Metallurgy and Materials Design Laboratory, Department of Mechanical Engineering and Materials Science, University of Pittsburgh, Pittsburgh, PA 15261

study the addition of Ti as an alternative path in HEA design, especially if the low-density for high-temperature applications are considered as the highest priority. So far, contrary to the Al-Co-Cr-Fe-Ni system, no studies have been reported on the Al-Co-Cr-Ni-Ti system. Therefore, three Al-Co-Cr-Ni-Ti HEAs are studied in this work to understand the process-microstructure-property relationships, which are indispensable for the development of the Al-Co-Cr-Ni-Fe-Ti alloy as the next step.

The ICME (Integrated Computational Materials Engineering) method offers engineers and scientists an efficient way for HEA design. As one of the supporting computational approaches for ICME, the CALPHAD method has been employed to predict phase stability, phase transformation temperature, phase composition and thermodynamic properties of HEAs,^[20–23] these properties are essential for alloy development and process optimization. In addition, *ab initio* calculations have also been utilized in HEA studies as a complementary tool, which can be used as the support for the CALPHAD modeling, especially when the pertinent experimental data are lacking.^[2,24–26] Although the *ab initio* approach has been extensively used in the theoretical calculations for alloys, the random mixing of the atoms of the solution phases in multicomponent HEA becomes one of the major obstacles for related energetic calculations. As another computational tool at the atomistic scale, molecular dynamics method can be employed to predict phase structure and atomic origins of phase transformation in HEAs,^[2,27,28] but the calculation efficiency is limited by the availability of the atomic potential. Recently, some promising results have been demonstrated by Huhn and Widom et al.,^[29,30] who developed a hybrid Monte Carlo/molecular dynamics method to predict the order/disorder phase transition^[29] and temperature-dependent chemical ordering effects^[30] of refractory HEAs.

Nevertheless, the CALPHAD approach, so far, is considered as one of the most efficient ways for HEA composition design and processing optimization over wide composition and temperature ranges.^[31,32] However, owing to the complexity of the multicomponent HEA systems, the reliability of the CALPHAD model-prediction should be evaluated, especially for the systems lacking reported experimental data.^[26,32] Therefore, one of the purposes of this work is to evaluate the uncertainty and limitations of the CALPHAD database TCHEA1 for the Al-Co-Cr-Ni-Ti HEA design modeling. The experimental data obtained in this work will further support the future improvement of the CALPHAD database of the Al-Co-Cr-Ni-Ti system.

2 Experiments

In total, three button alloys were arc-melted in a copper crucible under an argon atmosphere (Arc-Melter ABJ-338 manufactured by Materials Research Furnaces Inc.). These alloys are denoted as #1 ($\text{Al}_{0.1}\text{Co}_{0.2}\text{Cr}_{0.2}\text{Ni}_{0.2}\text{Ti}_{0.3}$), #2 ($\text{Al}_{0.2}\text{Co}_{0.2}\text{Cr}_{0.2}\text{Ni}_{0.2}\text{Ti}_{0.2}$) and #3 ($\text{Al}_{0.3}\text{Co}_{0.2}\text{Cr}_{0.2}\text{Ni}_{0.2}\text{Ti}_{0.1}$). Before the arc-melting, pure metals (purity > 99.95 wt.%) were weighted according to the elemental molar ratio in each alloy in a high-precision balance with uncertainty of 0.1 mg. Each alloy with weight about 10 g was re-melted for 5 times to ensure a high homogeneity with a total weight loss less than 0.5%. Afterward, one part of each as-cast sample was cut and encapsulated into quartz tubes under a vacuum condition with back-filled argon for isothermal annealing at 1193 K for 650 h (labeled as #1H, #2H and #3H). Another part of each as-cast sample was cut and encapsulated with the same way, whereas the samples were annealed at 1193 K for 1200 h (labeled as #1HL, #2HL and #3HL). After annealing, the quartz tubes with annealed samples were subject to quenching in ice-water as the final step to keep the phases achieved at 1193 K. It should be noted that the quartz tubes were broken in the ice-water to ensure the rapid cooling of alloy samples.

Crystal structures of different samples were identified by x-ray diffraction (XRD) on alloy powders using a Bruker D8 Discovery XRD System (Bruker AXS Inc., Madison, WI, USA) with Cu $K\alpha$ radiation, of which the wavelength is 1.54 nm. The scanning speed was chosen as 0.6°/min and 0.02°/step. Microstructure analysis and mechanical property measurements were performed on alloys under both as-cast and as-annealed states. Grain morphology and phase composition were determined using a ZEISS Sigma 500 VP scanning electron microscope (SEM) with Oxford Aztec energy dispersive x-ray spectroscopy (EDS). Phase volume fractions were estimated based on the two-dimensional microstructure images using the ImageJ software package. Vickers microhardness was determined using a Leco LM-800 tester under a 50 g load for 10 s.

3 Thermodynamic Models

In this work, the TCHEA1 database^[33] developed by the Thermo-Calc software AB is applied for the CALPHAD-type thermodynamic evaluation on phase stability of the prepared HEAs. Thermodynamic parameters are encrypted, and thus are not available for report. And this is one of the driving forces to evaluate the reliability of the TCHEA1 database. However, all of the phases in the TCHEA1 database are modeled within the framework of compound

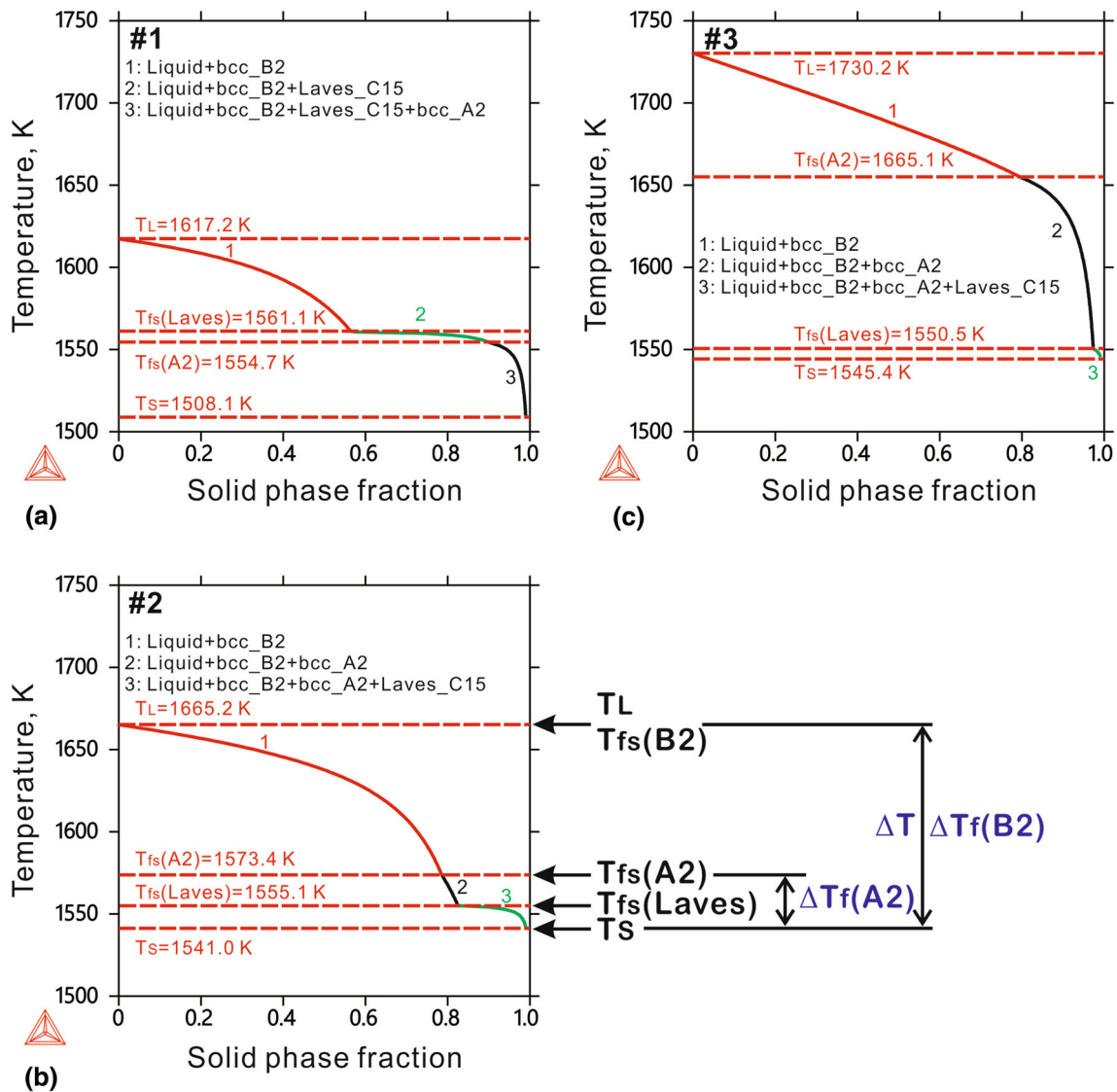


Fig. 1 Non-equilibrium solidification paths predicted by Scheil–Gulliver modeling for (a) sample #1; (b) sample #2; and (c) sample #3

energy formalism.^[34] The solution models are used for the liquid and solid solution phases. As an example, the Gibbs free energy of the bcc_A2 solution can be expressed as:

$$G_m^{A2} = \sum_i^c x_i^0 G_i^{A2} + RT \sum_i^c x_i \ln x_i + G_m^{ex} \quad (\text{Eq 1})$$

where G_m^{A2} is the molar Gibbs free energy of the bcc_A2 phase, c is the number of components, x_i is the mole fraction of component i , $^0 G_i^{A2}$ is the Gibbs free energy of component i in the bcc_A2 phase, G_m^{ex} is the excess Gibbs free energy, which can be described using the Redlich–Kister polynomials^[35] and the Muggianu extrapolation.^[36] Generally, the intermetallic phases such as Laves phase can be described using the sublattice model developed by Hillert et al.^[37–39] In addition, the ordered structure such as the bcc_B2 phase is described using the order–disorder

transition model, which has been extensively described by Sundman et al.^[40]

The nonequilibrium Scheil–Gulliver model^[41,42] is applied to predict solidification paths and phase composition in the as-cast alloys. Moreover, equilibrium calculations were performed to understand the microstructure after long-time annealing at 1193 K for 1200 h.

4 Results and Discussions

4.1 Solidification Microstructure of As-Cast Samples

As shown in Fig. 1, the Scheil–Gulliver modeling indicates that bcc_B2 is the primary solidification phase in all three

Table 1 Calculated formation temperature ranges (in Kelvin) according to the Scheil–Gulliver modeling

Alloy	Al/Ti ratio	T_S	Bcc_B2*		Bcc_A2		Laves_C15	
			T_L	ΔT	$T_{fs}(A2)$	$\Delta T_f(A2)$	$T_{fs}(Laves)$	$\Delta T_f(Laves)$
#1	1:3	1508.1	1617.2	109.1	1554.7	46.6	1561.1	53.0
#2	1:1	1541.0	1665.2	124.2	1573.4	32.4	1555.1	14.1
#3	3:1	1545.4	1730.2	184.8	1665.1	119.7	1550.5	5.1

* $T_L = T_{fs}(B2)$, and $\Delta T = \Delta T_f(B2)$

alloys, and bcc_A2 and Laves_C15 phases form subsequently. Moreover, the Laves_C15 phase forms as the secondary solidification phase in alloy #1 while the bcc_A2 forms secondarily in alloys #2 and #3. In order to better understand the phase behavior in solidification, some critical temperatures are defined for analysis. Although the freezing range ΔT , can be defined as $T_L - T_S$, which is the difference between the liquidus T_L and solidus T_S temperatures, a generic notation as shown in Fig. 1(b) is used to represent temperature ranges of phase formations during solidification. For example, T_{fs} is used to represent the starting temperatures of solid phase formation. In this case, $T_{fs}(B2) = T_L$ is considered for the bcc_B2 phase. Therefore, $\Delta T_f(B2) = T_{fs}(B2) - T_S$ is defined as the formation temperature range of the bcc_B2 phase. According to the Scheil–Gulliver modeling, the freezing range of all three alloys, ΔT , is equivalent to the formation temperature range of the bcc_B2 phase, i.e. $\Delta T = \Delta T_f(B2)$.

All of the above formation temperature ranges for different solid phases are summarized in Table 1. Both T_L and T_S increase with higher Al/Ti content ratio, although one would expect a decrease of the melting temperature from alloy #1 to #3 due to the reduction of Ti, which has a much higher melting temperature than Al. Figure 2 is the vertical section plotted between $Co_{0.2}Cr_{0.2}Ni_{0.2}Ti_{0.4}$ and $Al_{0.4}Co_{0.2}Cr_{0.2}Ni_{0.2}$, which presents a monotonic increase of the liquidus temperature from alloy #1 $Al_{0.1}Co_{0.2}Cr_{0.2}Ni_{0.2}Ti_{0.3}$ to #3 $Al_{0.3}Co_{0.2}Cr_{0.2}Ni_{0.2}Ti_{0.1}$.

In addition, the increasing Al/Ti ratio from alloy #1 to #3 also leads to a higher formation starting temperature of the bcc_A2 phase, $T_{fs}(A2)$. The formation temperature range $\Delta T_f(A2)$ of alloy #3 is the largest among all three alloys, and it indicates a long transformation duration of the bcc_A2 phase under solidification, which allows the grain to grow and coarsen sufficiently. The formation temperature range of different solid phases may explain the morphology of bcc_A2 phase in the solidified microstructure in different samples. For example, the lamella-shape bcc_A2 phase co-exists with bcc_B2 in both alloys #1 and #2, (see Fig. 3a and d), while only blocky grains can be observed in alloy #3 (see Fig. 3g) due to a wider formation temperature range $\Delta T_f(A2)$.

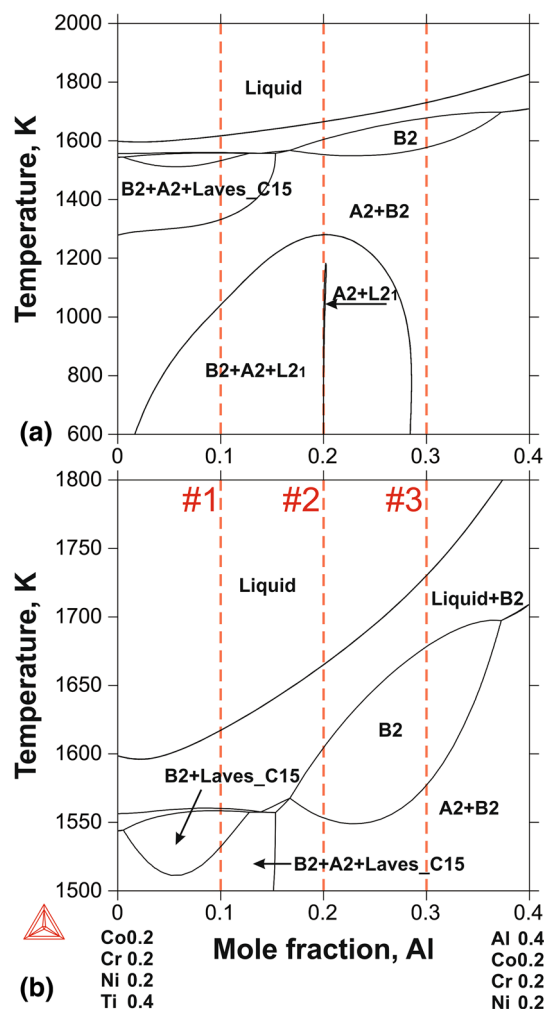


Fig. 2 Vertical section plotted between $Co_{0.2}Cr_{0.2}Ni_{0.2}Ti_{0.4}$ and $Al_{0.4}Co_{0.2}Cr_{0.2}Ni_{0.2}$ of the Al-Co-Cr-Ni-Ti alloy system. Plot in subfigure (b) is the magnification of (a)

The Scheil–Gulliver model-prediction on bcc_A2 and bcc_B2 formation is consistent with the microstructure observation shown in Fig. 3(a), (d), and (g) and XRD patterns given in Fig. 4. Regarding the Laves_C15 phase, it is predicted to form in all three alloys by Scheil–Gulliver model, while it was not observed in any of these alloys experimentally. In fact, the calculations listed in Table 1 indicate an insufficient formation temperature range in both alloy #2 (14.1 K) and #3 (5.1 K). Therefore, it is quite

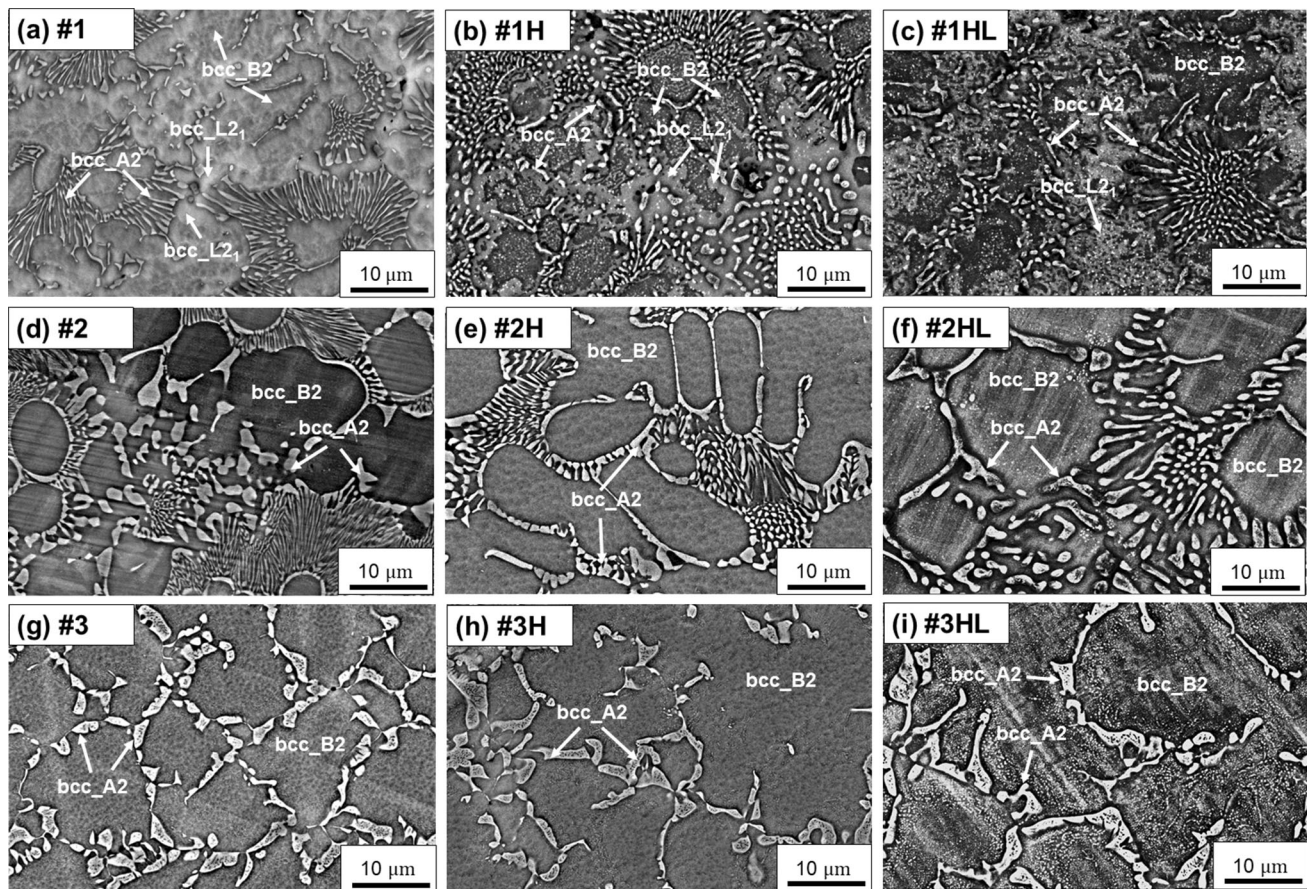


Fig. 3 SEM micrographs of as-cast samples: (a) #1; (d) #2; (g) #3, samples annealed at 1193 K for 650 h: (b) #1H; (e) #2H; (h) #3H, and 1200 h (c) #1HL; (f) #2HL; (i) #3HL

likely that the formation of Laves phase is kinetically prohibited. Although the predicted formation temperature range $\Delta T_f(\text{Laves})$ of the Laves_C15 phase in alloy #1 is relatively large (53 K), the formation of Laves_C15 phase is still not found in experiment. It is probable that the phase stability of Laves phase in this case is overestimated by the thermodynamic prediction. Contrarily, according to the comparison between modeling results in Fig. 1 and experimental observation in Fig. 3 and 4, the Scheil–Gulliver modeling underestimates the phase stability of the bcc_L2₁ phase in the solidification microstructure of alloy #1.

As an alternative way to validate the accuracy of the CALPHAD model-prediction, the phase compositions predicted by the Scheil–Gulliver model are compared with EDS results of as-cast alloys in Fig. 5. In principle, reasonable agreements between modeling and EDS results can be obtained, and the model-prediction is more accurate for the case in alloy #3 than #1. In alloy #1 and #2, better prediction on phase composition can be found in bcc_B2 than bcc_A2. The relatively large discrepancy in the bcc_A2 phase composition between calculations and

experiments for alloy #1 (Fig. 5b) is mainly due to the formation of Laves_C15 phase predicted by Scheil–Gulliver model. The formation of Laves phase changes the remaining liquid composition during Scheil–Gulliver modeling and leads to a more pronounced deviation from the real case. Besides, the absence of bcc_L2₁ phase in the calculation also affects the accuracy of the prediction. Regarding the bcc_A2 phase in alloy #2 (Fig. 5d), the model-predicted concentrations of Cr, Al, and Co agree well with measurements. However, for Ti, and especially Ni, the experimental values are much higher than predicted ones. The inconsistency indicates the room to further improve the accuracy of the HEA database.

The phase compositions obtained from calculations and experiments are summarized in Tables 2, 3 and 4. The bcc_B2 phase is rich in Co, Ni and Ti, but with a depletion of Cr. The bcc_L2₁ phase is a Heusler type structure (prototype: Ti₂NiCo) with its composition similar to the bcc_B2 phase. However, different with the case in the bcc_B2 phase, Al but not Cr is the depleted in bcc_L2₁ phase. The bcc_A2 phase is Cr-rich, which indicates the redistribution of Cr during the solidification processes.

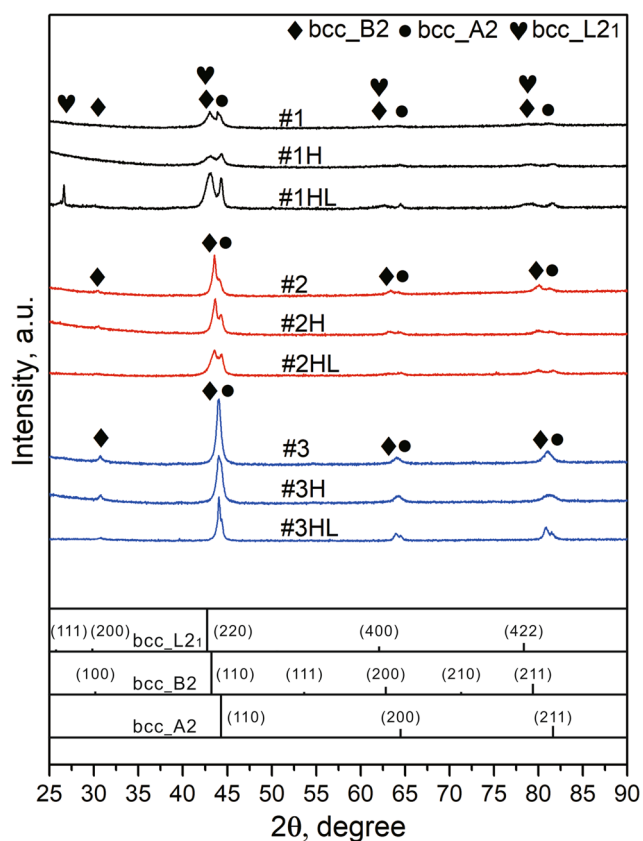


Fig. 4 XRD patterns of as-cast samples (#1, #2, & #3) and the ones annealed at 1193 K for 650 h (#1H, #2H, & #3H) and 1200 h (#1HL, #2HL, & #3HL). In the diffraction pattern of sample #1HL, the peak occurring $2\theta = 26.6^\circ$ is due to the quartz contamination during sample preparation, while the peak of (111) plane of L₂₁ phase locates in $2\theta = 26.3^\circ$, which is close to the quartz peak

4.2 Phase Stability Evaluation for Annealed Samples

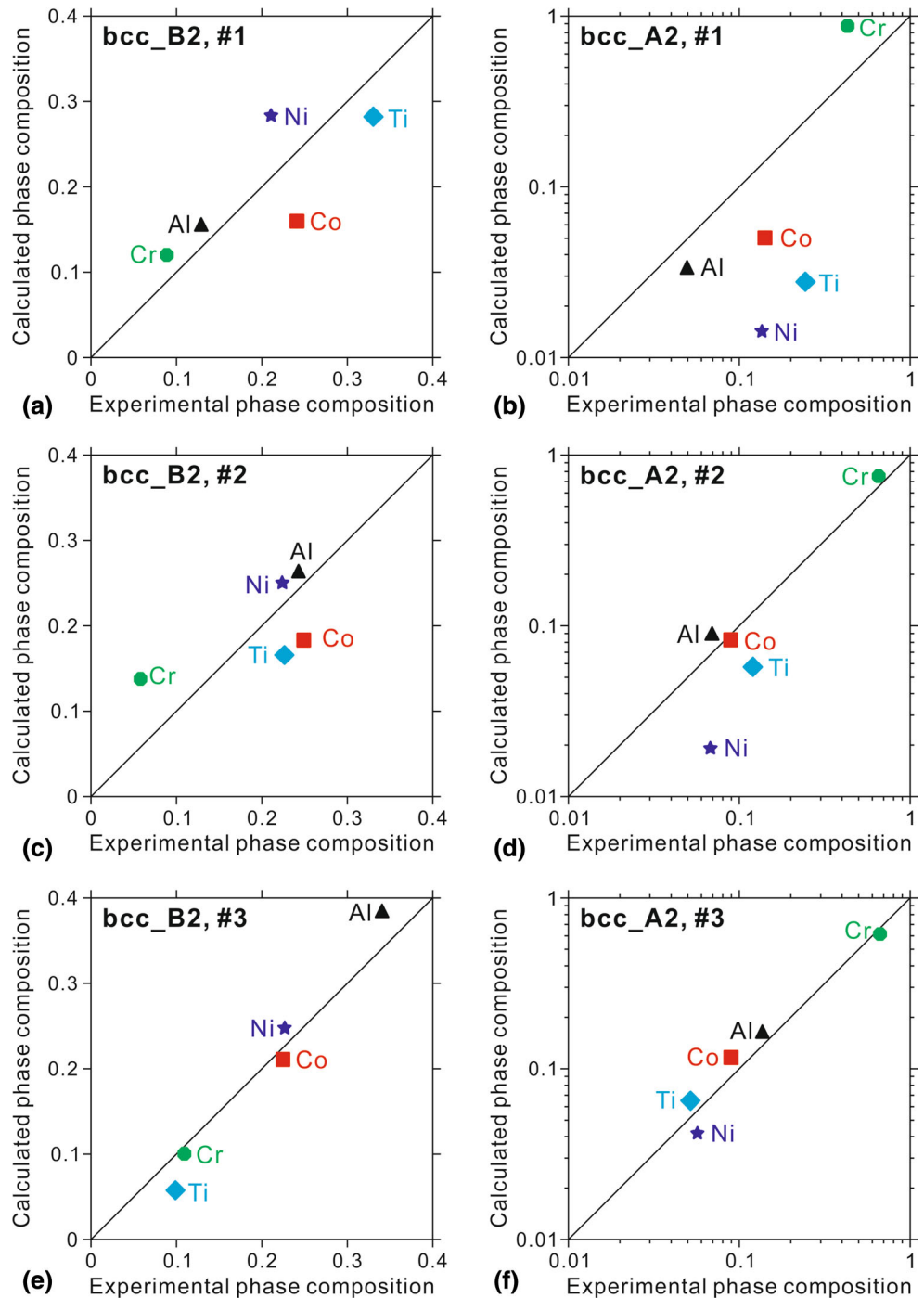
As shown in Fig. 6, the phase equilibrium calculations are performed to gain valuable insights into the phase stability in samples annealed at 1193 K for 1200 h, i.e. #1HL, #2HL, and #3HL. According to the microstructure analysis by SEM, the phase fraction was estimated using the two-dimensional images and compared with the model-prediction in Fig. 6. Therefore, it is difficult to evaluate the uncertainty of the estimation on phase fraction. Nevertheless, the difference between experimental estimation and model-prediction is significantly larger in the case of bcc_L₂₁ by comparing with the ones of bcc_A₂ and bcc_B₂. For sample #1HL, bcc_L₂₁ phase is observed in experiments (Fig. 3c) but not predicted by the calculation (Fig. 6a). Although the equilibrium calculations shown as the solid curves in Fig. 6(b) predict the existence of the bcc_L₂₁ phase in sample #2HL at 1193 K, it is not supported by both microstructures in Fig. 3(f) and XRD pattern in Fig. 4. Instead, the nonequilibrium calculations as

depicted by the dashed curve in Fig. 6(b) by excluding the bcc_L₂₁ phase agree well with the experimentally estimated phase fractions of bcc_A₂ and bcc_B₂.

The experimental and calculated volume percentages for each phase are listed in Table 5. Evidently, the bcc_L₂₁ phase fraction of alloy #1 increases significantly after annealing, which explains the observation of more distinct phase boundaries in the microstructure in Fig. 3(b) and (c). According to the experimental analysis, the bcc_B₂ phase fraction in alloy #1 decreases significantly after annealing, while a slight increase in the bcc_A₂ phase fraction can be observed after isothermal annealing. In the case of alloy #2, the bcc_B₂ fraction slightly decreases after annealing according to both experiments and calculations summarized in Table 5. However, since the Scheil–Gulliver model-prediction shows a considerable amount of Laves_C15, which cannot be observed by SEM, the agreement of the bcc_A₂ phase between calculations and experimental estimation on as-cast samples is less satisfied. Similar cases can be found in Table 5 for alloy #3. According to the comparison in Fig. 6 and Table 5, it can be concluded that the CALPHAD model is more reliable in predicting the phase fractions of bcc_A₂ and bcc_B₂ than bcc_L₂₁.

The phase compositions in the as-annealed alloys are summarized in Fig. 7, and the comparison shows a reasonable agreement between experiments and CALPHAD model-prediction for both bcc_A₂ and bcc_B₂ phases. Nevertheless, the agreement between CALPHAD model prediction and experiments in bcc_A₂ phase is not as good as that in bcc_B₂ phase, as can be found in Fig. 7(b), (d) and (f), especially for Co and Ti. If we assume the long-time annealing (1200 h) is sufficiently long enough to reach the close-equilibrium states in the experiment, the discrepancies observed in the phase composition indicate the lack of accuracy of the thermodynamic model-prediction. It is understandable that since the bcc_L₂₁ phase is not predicted by the thermodynamic calculations for alloy #1, the accuracy of the model-prediction on bcc_A₂ phase composition can be affected consequently. However, considering bcc_A₂ only occurs as the minor phase in these alloys, and the CALPHAD database can reasonably predict the Cr content as the major component in the bcc_A₂ phase, the prediction is still valuable in guiding the HEA development. More detailed information of phase composition in different alloys is summarized in Tables 2, 3 and 4. The small differences in phase compositions between alloys annealed for 650 h and 1200 h confirm the sluggish diffusion and high phase stability of these HEAs. Although a considerable reduction of the bcc_B₂ phase fraction in alloy #1 is found after 650 h annealing, the phase compositions keep invariant in different annealing states as shown in Table 2.

Fig. 5 Comparison of phase composition in as-cast alloys between the Scheil–Gulliver model-prediction and EDS measurements. (a) the bcc_B2 phase of alloy #1; (b) the bcc_A2 phase of alloy #1; (c) the bcc_B2 phase of alloy #2; (d) the bcc_A2 phase of alloy #2; (e) the bcc_B2 phase of alloy #3; and (f) the bcc_A2 phase of alloy #3



Overall, the CALPHAD predicted phase stability and compositions of bcc_A2 and bcc_B2 phases agree with experimental observation. However, the model shows the insufficient accuracy of the prediction on bcc_L2₁. As discussed in Fig. 6, the model underestimates the bcc_L2₁ phase stability for the case of sample #1HL, but overestimates it for #2HL. Therefore, a better description of bcc_L2₁ phase is desired in the future improvement of the thermodynamic database.

4.3 XRD Analysis Assisted by the CALPHAD Molar Volume Database

As shown in Fig. 4, the phase identification by XRD is consistent with the microstructure analysis. Both bcc_A2 and bcc_B2 phases can be identified in all samples, whereas bcc_L2₁ phase is found in alloy #1 under both as-cast and annealed conditions. Broader peaks are observed in sample #1, indicating they may have the more

Table 2 Phase composition for alloy #1

#1	At.%	Al		Co		Cr		Ni		Ti	
		Exp.	Calc.								
B2	#1	12.90	15.42	24.10	15.97	8.87	12.02	21.08	28.37	33.05	28.21
	#1H	15.05	...	24.35	...	5.42	...	24.46	...	30.72	...
	#1HL	15.54	11.89	21.52	24.31	6.70	2.91	24.60	24.38	31.65	36.50
A2	#1	4.95	3.31	14.12	5.03	42.99	87.46	13.54	1.43	24.40	2.78
	#1H	2.48	...	11.04	...	61.47	...	8.47	...	16.54	...
	#1HL	2.47	1.38	7.24	0.35	69.90	97.81	6.25	0.00	14.13	0.43
L2 ₁	#1	6.57	...	19.04	...	10.59	...	26.02	...	37.78	...
	#1H	7.07	...	26.72	...	8.71	...	21.77	...	35.73	...
	#1HL	7.56	...	24.57	...	8.08	...	21.07	...	38.72	...

Table 3 Phase composition for alloy #2

#2	At.%	Al		Co		Cr		Ni		Ti	
		Exp.	Calc.								
B2	#2	24.29	26.24	24.90	18.33	5.79	13.79	22.39	25.05	22.63	16.58
	#2H	23.91	...	24.85	...	5.33	...	22.91	...	23.00	...
	#2HL	25.51	23.46	24.14	23.93	4.70	4.57	22.97	24.04	22.69	23.99
A2	#2	6.92	8.85	8.90	8.28	65.40	75.20	6.78	1.92	12.00	5.75
	#2H	4.43	...	7.64	...	74.69	...	4.98	...	8.27	...
	#2HL	3.17	2.89	5.26	0.58	81.19	96.20	3.82	0.03	6.56	0.29

Table 4 Phase composition for alloy #3

#3	At.%	Al		Co		Cr		Ni		Ti	
		Exp.	Calc.								
B2	#3	34.05	38.32	22.47	21.08	10.93	10.05	22.66	24.79	9.89	5.77
	#3H	33.22	...	22.70	...	11.11	...	22.76	...	10.22	...
	#3HL	35.46	35.34	21.79	24.09	11.00	4.26	21.98	24.23	9.76	12.08
A2	#3	13.65	16.17	8.94	11.64	66.54	61.49	5.69	4.20	5.18	6.49
	#3H	12.63	...	10.04	...	65.32	...	7.18	...	4.83	...
	#3HL	11.77	4.82	8.89	0.71	68.94	94.26	6.20	0.03	4.20	0.18

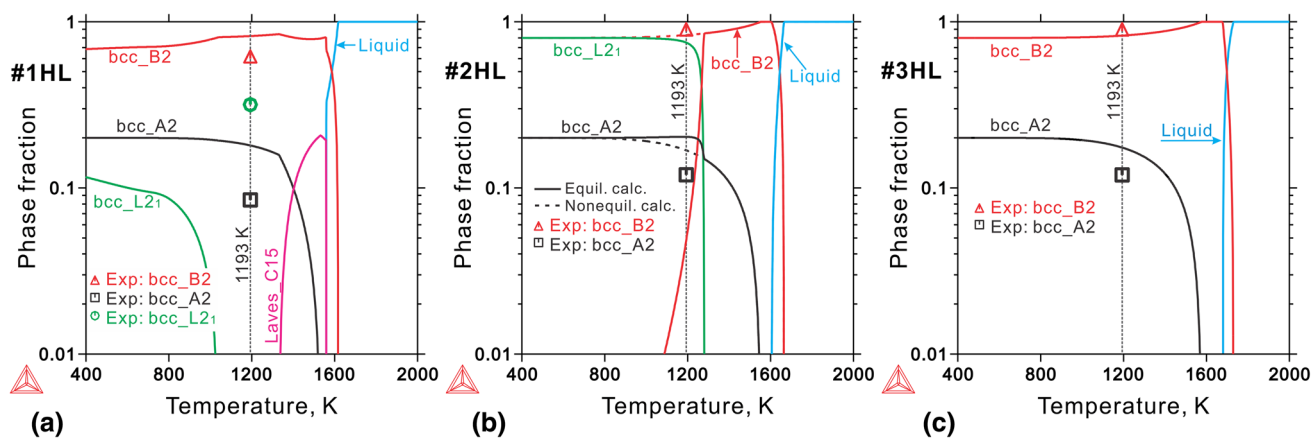


Fig. 6 Comparison of phase fraction between CALPHAD equilibrium calculation and experimental analysis for alloys isothermally annealed at 1193 K for 1200 h (a) #1HL; (b) #2HL; and (c) #3HL

Table 5 Comparison of phase volume percentage between experimental estimation and CALPHAD calculation for both as-cast and annealed samples

Alloy no.	Bcc_B2		Bcc_A2		Bcc_L2 ₁		Laves_C15	
	Exp.	Calc.*	Exp.	Calc.	Exp.	Calc.	Exp.	Calc.
#1	80.44	74.41	6.92	0.91	12.64	23.69
#1H	61.17	...	7.83	...	31.00
#1HL	60.64	83.35	8.30	16.65	31.06	0
#2	90.18	88.06	9.82	2.37	8.61
#2H	90.15	...	9.85
#2HL	88.23	83.94	11.77	16.06	0
#3	88.67	95.33	11.33	2.88	0.09
#3H	88.06	...	11.94
#3HL	88.25	82.78	11.75	17.22	0

*CALPHAD equilibrium calculation is used for comparing with the experimental analysis on annealed samples at 1193 K for 1200 h (#1HL, #2HL, and #3HL)

pronounced lattice distortion. For the as-cast samples, the peaks of the bcc_A2 and bcc_B2 phases are more distinct in alloys #1 and #2, whereas the peaks of both phases overlap in alloy #3. A similar trend of the overlapping XRD peaks can also be observed in the as-annealed cases.

The overlapping peaks such as the ones in sample #3 may be due to the close lattice constants of bcc_A2 and bcc_B2 phases. Therefore, in order to further assist the XRD analysis, the CALPHAD molar volume database is applied to estimate the 2θ value through the calculations of the lattice constants. In this work, the lattice constants of the equilibrium phases are estimated from the Thermo-Calc TCHEA1 database, and the calculations are performed on samples #1HL, #2HL, and #3HL, since the long-time annealed alloys are considered approaching to the equilibrium state.

As an example, the calculated molar volumes of bcc_A2 and bcc_B2 phases are employed to determine the corresponding Bragg's angle of (110) peak, for which the overlapping is noticeable in all three alloys (see Fig. 4). The relationship between the lattice constant of bcc phase, *a*, can be expressed as:

$$a = \left(\frac{2V_m}{N_A} \right)^{\frac{1}{3}} \tag{Eq 2}$$

where *V_m* is the molar volume of the phases, and thus can be directly achieved from the CALPHAD molar volume database, and *N_A* is the Avogadro constant. According to the Bragg's law,^[43] the 2θ value for (110) plane can be expressed as:

$$2\theta = 2 \sin^{-1} \left(\frac{\lambda}{2d_{110}} \right) \tag{Eq 3}$$

where λ is the wavelength of Cu Kα x-ray of which the value is 1.5406 × 10⁻¹⁰ m, *d₁₁₀* is the interplanar spacing

between the (110) planes, which is equal to *a*/√2 for the bcc structure.

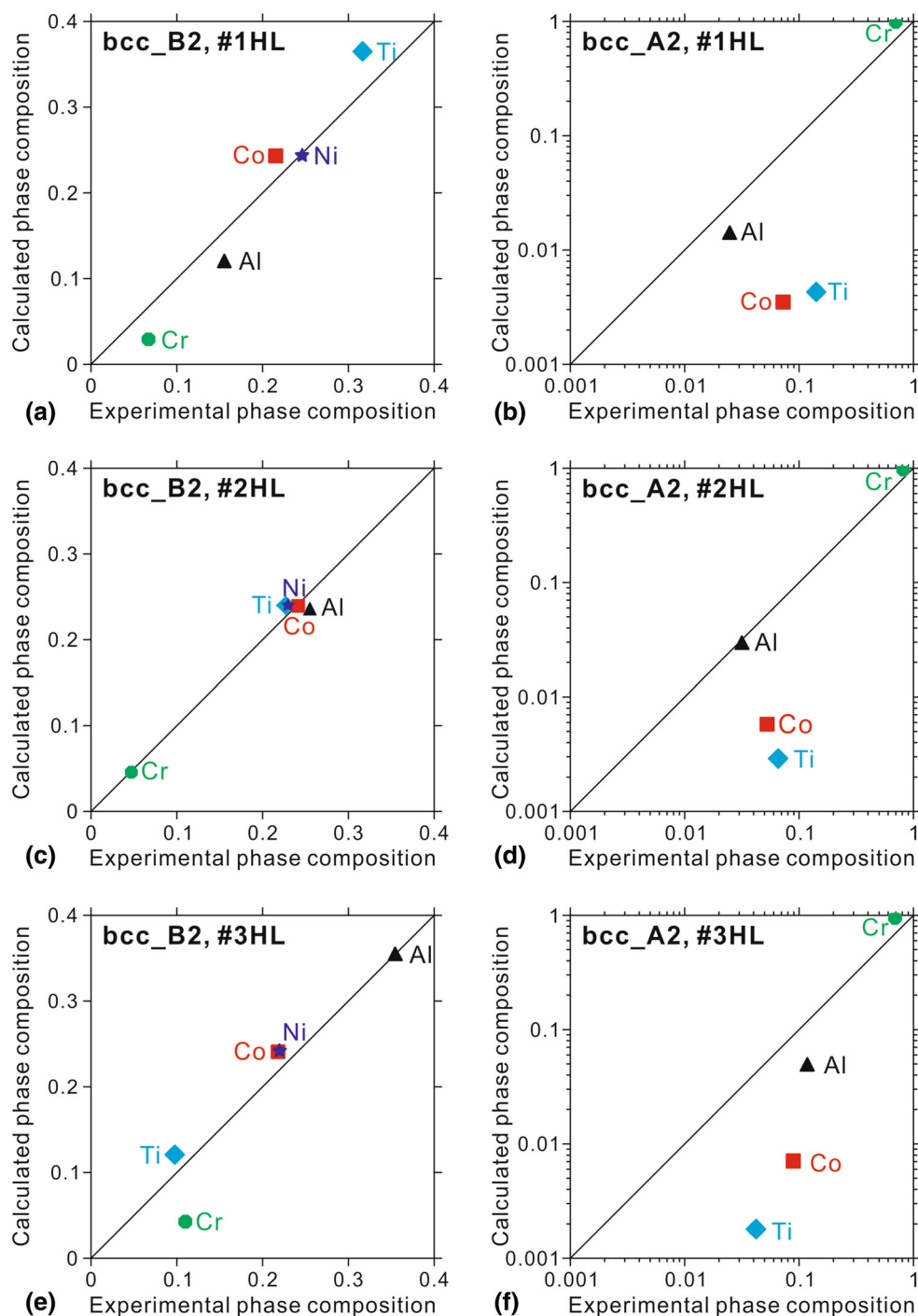
The calculated and experimental 2θ values differences between bcc_A2 and bcc_B2 phases, Δ2θ, for all three long-time as-annealed samples are given in Table 6. Since the calculated lattice constants of bcc_A2 and bcc_B2 phases are closer in sample #3HL, the corresponding Δ2θ values are thus smaller, which leads to the peak overlapping. In addition, the experimental Δ2θ value between bcc_A2 and bcc_B2 phases decreases from sample #1HL to #3HL. This can be confirmed from the CALPHAD-based calculations as shown in Table 6.

4.4 Heat Treatment-Microstructure-Hardness Relationships

Figure 8 presents the Vickers hardness of three alloys under both as-cast and annealed conditions. According to the information indicated in Table 5, Fig. 3 and 8, since phase fraction and grain morphology show the least change for alloy #3 before and after isothermal annealing, the hardness of alloy #3 also has the least variation by comparing with alloys #1 and #2. The reduction of the hardness of alloy #2 shown in Fig. 8 may be due to the combined effects of a reduction in the volume of the A2 + B2 lamella structure with increased interlamellar spacing, because the volume of both bcc_A2 and bcc_B2 phases does not change significantly in alloy #2 before and after annealing as summarized in Table 5. By comparing with the case in alloy #2, the change of the morphology with the A2 + B2 lamella structure in alloy #1 is less pronounced. Instead the decrease of the bcc_B2 phase fraction and the simultaneous increase of bcc_L2₁ could be the main contributions to the softening effects observed in alloy #1.

Overall, the microhardness of the as-cast samples decreases with the increase of Al/Ti ratio from sample #1

Fig. 7 Comparison between CALPHAD calculated and experimental measured phase composition of annealed samples (a) bcc_B2, #1HL; (b) bcc_A2, #1HL; (c) bcc_B2, #2HL; (d) bcc_A2, #2HL; (e) bcc_B2, #3HL; and (f) bcc_A2, #3HL



to #3. This may be due to the reduction of the A2 + B2 lamella structure, which can enhance the hardness as long as the interlamellar spacing is moderately small. In addition, it is reasonable to conclude that the bcc_B2 phase also contributes significantly to the hardness, because both alloys #2 and #3 retain comparable hardness with alloy #1 after annealing, although samples #2H and #2HL show a coarse A2 + B2 lamella structure, and samples #3H and #3HL do not have the lamella structure even.

Due to the high value of the hardness observed in the studied HEAs, one potential application could be the laser cladding HEA coating, which is one of the underdeveloped areas receiving more research focus due to the development of additive manufacturing and HEAs. In this work, the density variation as a function of temperature is calculated based on the Thermo-Calc TCHEA1 database as shown in Fig. 9(a). According to the materials property space for room-temperature hardness versus density of

Table 6 Comparison of calculated and experimental 2θ values for (110) planes

	V_m (m ³), CALPHAD		a (m)		2θ ($^\circ$), calc.			2θ ($^\circ$), exp.		
	A2	B2	A2	B2	A2	B2	$\Delta 2\theta$	A2	B2	$\Delta 2\theta$
#1HL	7.454E-6	8.194E-6	2.915E-10	3.008E-10	43.90	42.47	1.43	44.27	43.17	1.10
#2HL	7.484E-6	7.917E-6	2.918E-10	2.974E-10	43.84	42.98	0.86	44.37	43.55	0.82
#3HL	7.524E-6	7.664E-6	2.924E-10	2.942E-10	43.75	43.47	0.28	44.35	44.07	0.28

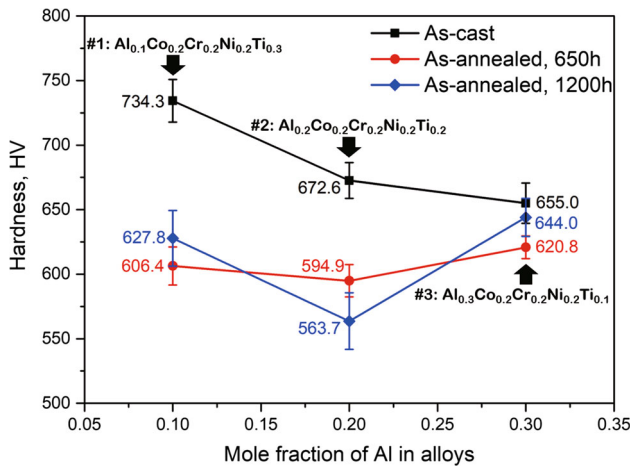
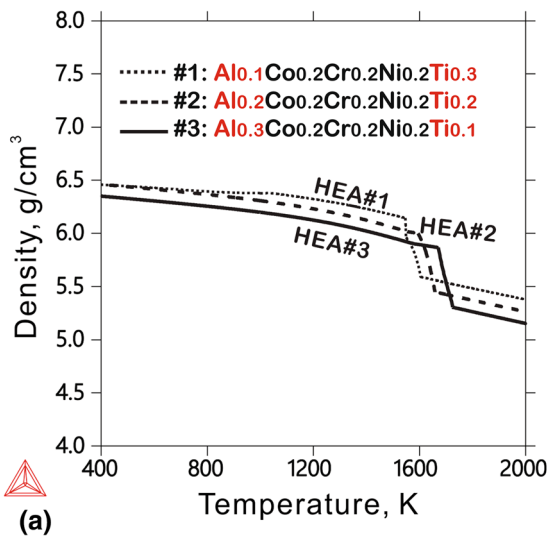


Fig. 8 Vickers hardness of $Al_xCo_{0.2}Cr_{0.2}Ni_{0.2}Ti_{0.4-x}$ under as-cast and annealed conditions

laser cladding HEA coatings^[44] presented in Fig. 9(b), the Al-Co-Cr-Ni-Ti HEAs can be considered as one of the outstanding candidate materials for light-weight high-temperature applications.



5 Concluding Remarks

1. The CALPHAD thermodynamic database TCHEA1 can reasonably predict the phase stability in the Al-Co-Cr-Ni-Ti alloys under the as-cast and equilibrium conditions. The CALPHAD calculations predict the presence of bcc_B2 as the major phase and bcc_A2 as the minor phase in all $Al_xCo_{0.2}Cr_{0.2}Ni_{0.2}Ti_{0.4-x}$ HEAs studied in this work. The comparison between model-prediction and experiments shows better agreement on bcc_A2 and bcc_B2 phases. An improved thermodynamic description of the bcc_L2₁ phase is needed for the TCHEA1 database. Further development of the CALPHAD HEA database is critical to the success of the HEA development.
2. The higher Al/Ti ratio of the $Al_xCo_{0.2}Cr_{0.2}Ni_{0.2}Ti_{0.4-x}$ alloys could increase the solidification temperature ranges and solidus temperatures of HEAs during solidification processes. The hardening effect of bcc_B2 phase in as-cast HEAs can be enhanced by the reduction of Al/Ti ratio.

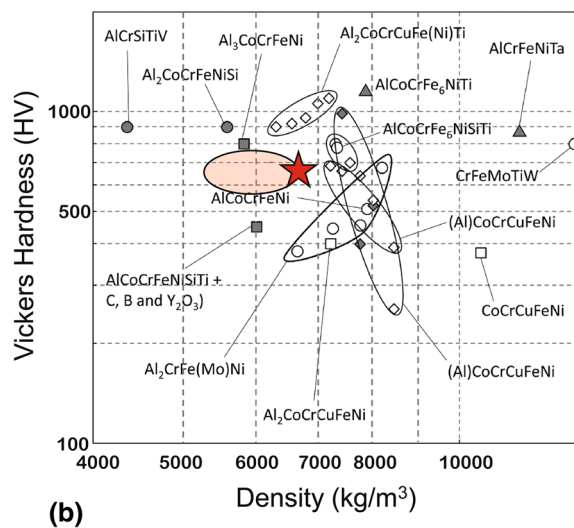


Fig. 9 (a) Density variation vs. temperature of the HEAs studied in this work. (b) Ashby plot of the materials property space for hardness vs. density of laser cladding HEA coatings. The shadowed area represents

the possible density range that can be achieved for the Al-Co-Cr-Ni-Ti alloys. The red star marks the room-temperature hardness range of the three alloys studied in this work (Color figure online)

3. Both bcc_B2 matrix and A2 + B2 lamella structure may contribute to the hardness of the HEAs studied in this work. However, the A2 + B2 lamella structure requires a fine interlamellar spacing to reserve such a contribution. Generally, long-time annealing can promote the formation of the Cr-rich bcc_A2 phase and increase the interlamellar spacing, and this will result in the decrease of hardness.
4. The CALPHAD molar volume database can be used for the XRD analysis gaining useful insight into the overlapping XRD peaks due to similar lattice constants. The combined analysis of XRD, SEM/EDS and microhardness indicates sluggish kinetics of the studied HEAs.
5. Due to the high specific hardness, the Al-Co-Cr-Ni-Ti HEAs can be potentially applied as the light-weight laser cladding HEA coatings.

Acknowledgments We are grateful for the financial support of the U.S. Nuclear Regulatory Commission under Award Number (NRC-HQ-84-15-G-0029). The authors thank the support of the ThermoCalc company for the CALPHAD computation using the ThermoCalc software and databases.

References

1. J.W. Yeh, S.K. Chen, S.J. Lin, J.Y. Gan, T.S. Chin, T.T. Shun, C.H. Tsau, and S.Y. Chang, Nanostructured High-Entropy Alloys with Multiple Principal Elements: Novel Alloy Design Concepts and Outcomes, *Adv. Eng. Mater.*, 2004, **6**(5), p 299-303
2. B.S. Murty, J.-W. Yeh, and S. Ranganathan, *High-Entropy Alloys*, Butterworth-Heinemann, Oxford, 2014
3. Y.Y. Chen, T. Duval, U.D. Hung, J.W. Yeh, and H.C. Shih, Microstructure and Electrochemical Properties of High Entropy Alloys—a Comparison with Type-304 Stainless Steel, *Corros. Sci.*, 2005, **47**(9), p 2257-2279
4. C.-J. Tong, Y.-L. Chen, J.-W. Yeh, S.-J. Lin, S.-K. Chen, T.-T. Shun, C.-H. Tsau, and S.-Y. Chang, Mechanical Performance of the Al_xCoCrCuFeNi High-Entropy Alloy System with Multiprincipal Elements, *Metall. Mater. Trans. A*, 2005, **36**(4), p 881-893
5. K.B. Zhang, Z.Y. Fu, J.Y. Zhang, J. Shi, W.M. Wang, H. Wang, Y.C. Wang, and Q.J. Zhang, Annealing on the Structure and Properties Evolution of the CoCrFeNiCuAl High-Entropy Alloy, *J. Alloys Compd.*, 2010, **502**(2), p 295-299
6. C. Ng, S. Guo, J. Luan, S. Shi, and C.T. Liu, Entropy-Driven Phase Stability and Slow Diffusion Kinetics in an Al_{0.5}CoCrCuFeNi High Entropy Alloy, *Intermetallics*, 2012, **31**, p 165-172
7. X.W. Qiu, Y.P. Zhang, L. He, and C.G. Liu, Microstructure and Corrosion Resistance of AlCrFeCuCo High Entropy Alloy, *J. Alloys Compd.*, 2013, **549**, p 195-199
8. L.J. Santodonato, Y. Zhang, M. Feygenson, C.M. Parish, M.C. Gao, R.J.K. Weber, J.C. Neuefeind, Z. Tang, and P.K. Liaw, Deviation from High-Entropy Configurations in the Atomic Distributions of a Multi-Principal-Element Alloy, *Nat. Commun.*, 2015, **6**, p 1-13
9. Z. Li, K.G. Pradeep, Y. Deng, D. Raabe, and C.C. Tasan, Metastable High-Entropy Dual-Phase Alloys Overcome the Strength–ductility Trade-Off, *Nature*, 2016, **534**, p 4-11
10. K.S. Lee, J.H. Kang, K.R. Lim, and Y.S. Na, Influence of Compressive Strain on the Microstructural Evolution of an AlCoCrFeNi High Entropy Alloy, *Mater. Charact.*, 2017, **132**, p 162-168
11. J. Sato, T. Omori, K. Oikawa, I. Ohnuma, R. Kainuma, and K. Ishida, Cobalt-Base High-Temperature Alloys, *Science*, 2006, **312**(5770), p 90-91
12. T.M. Pollock, J. Dibbern, M. Tsunekane, J. Zhu, and A. Suzuki, New Co-Based γ - γ' High-Temperature Alloys, *JOM*, 2010, **62**(1), p 58-63
13. D. Furrer and H. Fecht, Ni-Based Superalloys for Turbine Discs, *JOM*, 1999, **51**(1), p 14-17
14. Z. Tang, O.N. Senkov, C.M. Parish, C. Zhang, F. Zhang, L.J. Santodonato, G. Wang, G. Zhao, F. Yang, and P.K. Liaw, Tensile Ductility of an AlCoCrFeNi Multi-Phase High-Entropy Alloy Through Hot Isostatic Pressing (HIP) and Homogenization, *Mater. Sci. Eng., A*, 2015, **647**, p 229-240
15. H. Zhang, Y. Pan, and Y.Z. He, Synthesis and Characterization of FeCoNiCrCu High-Entropy Alloy Coating by Laser Cladding, *Mater. Des.*, 2011, **32**(4), p 1910-1915
16. Y. Shi, B. Yang, and P. Liaw, Corrosion-Resistant High-Entropy Alloys: A Review, *Metals*, 2017, **7**(2), p 43
17. W.R. Wang, W.L. Wang, S.C. Wang, Y.C. Tsai, C.H. Lai, and J.W. Yeh, Effects of Al Addition on the Microstructure and Mechanical Property of Al_xCoCrFeNi High-Entropy Alloys, *Intermetallics*, 2012, **26**, p 44-51
18. Z. Tang, M.C. Gao, H. Diao, T. Yang, J. Liu, T. Zuo, Y. Zhang, Z. Lu, Y. Cheng, Y. Zhang, K.A. Dahmen, P.K. Liaw, and T. Egami, Aluminum Alloying Effects on Lattice Types, Microstructures, and Mechanical Behavior of High-Entropy Alloys Systems, *JOM*, 2013, **65**(12), p 1848-1858
19. X. Yang, Y. Zhang, and P.K. Liaw, Microstructure and Compressive Properties of NbTiVTaAl_x High Entropy Alloys, *Procedia Eng.*, 2012, **36**, p 292-298
20. A. Durga, K.C. Hari Kumar, and B.S. Murty, Phase Formation in Equiatomic High Entropy Alloys: CALPHAD Approach and Experimental Studies, *Trans. Indian Inst. Met.*, 2012, **65**(4), p 375-380
21. B. Zhang, M.C. Gao, Y. Zhang, and S.M. Guo, Senary Refractory High-Entropy Alloy Cr X MoNbTaVW, *Calphad*, 2015, **51**, p 193-201
22. M.C. Gao, C.S. Carney, Ö.N. Doğan, P.D. Jablonksi, J.A. Hawk, and D.E. Alman, Design of Refractory High-Entropy Alloys, *JOM*, 2015, **67**(11), p 2653-2669
23. W.-M. Choi, S. Jung, Y.H. Jo, S. Lee, and B.-J. Lee, Design of New Face-Centered Cubic High Entropy Alloys by Thermodynamic Calculation, *Met. Mater. Int.*, 2017, **23**(5), p 839-847
24. W. Xiong, Y. Du, R.-X. Hu, J. Wang, W.-W. Zhang, P. Nash, and X.-G. Lu, Construction of the Al–Ni–Si Phase Diagram over the Whole Composition and Temperature Ranges: Thermodynamic Modeling Supported by Key Experiments and First-Principles Calculations, *Int. J. Mater. Res.*, 2008, **99**(6), p 598-612
25. W. Xiong and G.B. Olson, Integrated Computational Materials Design for High-Performance Alloys, *MRS Bull.*, 2015, **40**(12), p 1035-1043
26. W. Xiong and G.B. Olson, Cybermaterials: Materials by Design and Accelerated Insertion of Materials, *NPJ Comput. Mater.*, 2016, **2**, p 15009
27. S. Maiti and W. Steurer, Structural-Disorder and Its Effect on Mechanical Properties in Single-Phase TaNbHfZr High-Entropy Alloy, *Acta Mater.*, 2016, **106**, p 87-97

28. A. Sharma, S.A. Deshmukh, P.K. Liaw, and G. Balasubramanian, Crystallization Kinetics in Al_xCrCoFeNi ($0 \leq X \leq 40$) High-Entropy Alloys, *Scr. Mater.*, 2017, **141**, p 54-57
29. W.P. Huhn and M. Widom, Prediction of A2 to B2 Phase Transition in the High-Entropy Alloy Mo-Nb-Ta-W, *JOM*, 2013, **65**(12), p 1772-1779
30. M. Widom, W.P. Huhn, S. Maiti, and W. Steurer, Hybrid Monte Carlo/molecular Dynamics Simulation of a Refractory Metal High Entropy Alloy, *Metall. Mater. Trans. A*, 2014, **45**(1), p 196-200
31. D.B. Miracle, J.D. Miller, O.N. Senkov, C. Woodward, M.D. Uchic, and J. Tiley, Exploration and Development of High Entropy Alloys for Structural Applications, *Entropy*, 2014, **16**(1), p 494-525
32. O.N. Senkov, J.D. Miller, D.B. Miracle, and C. Woodward, Accelerated Exploration of Multi-Principal Element Alloys with Solid Solution Phases, *Nat. Commun.*, 2015, **6**, p 6529
33. H. Mao, H.L. Chen, and Q. Chen, TCHEA1: A Thermodynamic Database Not Limited for "High Entropy" Alloys, *J. Phase Equilibria Diffus.*, 2017, **38**(4), p 353-368
34. Mats Hillert, The Compound Energy Formalism, *J. Alloys Compd.*, 2001, **320**, p 161-176
35. O. Redlich and A.T. Kister, Algebraic Representation of Thermodynamic Properties and the Classification of Solutions, *Ind. Eng. Chem.*, 1948, **40**(2), p 345-348
36. Y.M. Muggianu, M. Gambino, and J.P. Bros, Enthalpies of Formation of Liquid Alloys Bismuth-Gallium-Tin at 723 k-Choice of an Analytical Representation of Integral and Partial Thermodynamic Functions of Mixing for This Ternary-System, *J. Chim. Phys. Physico-Chimie Biol.*, 1975, **72**(1), p 83-88
37. M. Hillert and L.-I. Staffansson, The Regular Solution Model for Stoichiometric Phases and Ionic Melts, *Acta Chem. Scand.*, 1970, **24**, p 3618-3626
38. B. Sundman and J. Ågren, A Regular Solution Model for Phases with Several Components and Sublattices, Suitable for Computer Applications, *J. Phys. Chem. Solids*, 1981, **42**(4), p 297-301
39. B. Sundman and J. Ågren, The Sublattice Model, *MRS Proc.*, 1982, **19**, p 115
40. H.L. Lukas, S.G. Fries, and B. Sundman, *Computational Thermodynamics: The Calphad Method*, Cambridge University Press, Cambridge, 2007
41. G.H. Gulliver, The Quantitative Effect of Rapid Cooling upon the Constitution of Binary Alloys, *J. Inst. Met.*, 1913, **9**(1), p 120-157
42. E. Scheil, Bemerkungen Zur Schichtkristallbildung, *Zeitschrift für Met.*, 1942, **34**(3), p 70-72
43. W.H. Bragg and W.L. Bragg, The Reflection of X-Rays by Crystals, *Proc. R. Soc. A Math. Phys. Eng. Sci.*, 1913, **88**(605), p 428-438
44. S. Gorsse, C. Hutchinson, M. Gouné, and R. Banerjee, Additive Manufacturing of Metals: A Brief Review of the Characteristic Microstructures and Properties of Steels, Ti-6Al-4 V and High-Entropy Alloys, *Sci. Technol. Adv. Mater.*, 2017, **18**(1), p 584-610